Detecting Water Vapor Variability during Heavy Precipitation Events in Hong Kong Using the GPS Tomographic Technique

BIYAN CHEN AND ZHIZHAO LIU

Department of Land Surveying and Geo-Informatics, Hong Kong Polytechnic University, Hung Hom, Kowloon, Hong Kong, China

WAI-KIN WONG AND WANG-CHUN WOO

Hong Kong Observatory, Kowloon, Hong Kong, China

(Manuscript received 3 June 2016, in final form 13 January 2017)

ABSTRACT

Water vapor has a strong influence on the evolution of heavy precipitation events due to the huge latent heat associated with the phase change process of water. Accurate monitoring of atmospheric water vapor distribution is thus essential in predicting the severity and life cycle of heavy rain. This paper presents a systematic study on the application of tomographic solutions to investigate water vapor variations during heavy precipitation events. Using global positioning system (GPS) observations, the wet refractivity field was constructed at a temporal resolution of 30 min for three heavy precipitation events occurring in Hong Kong, China, in 2010–14. The zenith wet delay (ZWD) is shown to be a good indicator in observing the water vapor evolution in heavy rain events. The variabilities of water vapor at five altitude layers (<1000, 1000–2000, 2000–3000, 3000–5000, and >5000 m) were examined. It revealed that water vapor above 3000 m has larger fluctuation than that under 3000 m, though it accounts for only 10%–25% of the total amount of water vapor. The relative humidity fields derived from tomographic results revealed moisture variation, accumulation, saturation, and condensation during the heavy rain events. The water vapor variabilities observed by tomography have been validated using European Centre for Medium-Range Weather Forecasts (ECMWF) reanalysis and radiosonde data. The results positively demonstrated the potential of using water vapor tomographic technique for detecting and monitoring the evolution of heavy rain events.

1. Introduction

Modern cities are increasingly vulnerable to natural disasters such as thunderstorms, hailstorms, and tornados due to urbanization and population concentration in many developing countries, such as China. Over the past decades, a continued increase of greenhouse gas emissions due to anthropogenic activities has led to more frequent abnormalities in climatological parameters such as temperature, precipitation, and evapotranspiration (IPCC 2014). Global warming results in dramatic impacts on regional climate, and it is observed that the frequency and intensity of extreme precipitation in some regions have been escalating, implying greater proneness to the risk of flooding (IPCC 2014). Flash flooding and landslides triggered by high-intensity rainfall can result in catastrophic casualties as well as significant damages to urban infrastructure and agricultural production, especially for highly populated and less developed regions (Pilon 2005; Chang and Guo 2006; Jessup and DeGaetano 2008; Kawano et al. 2008). Consequently, reliable forecasting of the development and life cycle of extreme precipitation events is of great significance for natural hazard mitigation in urban regions.

All the basic weather phenomena we experience everyday such as cloud, drizzle, rain, snow, sleet, and hail are intimately associated with atmospheric water vapor (Mohanakumar 2008; Ahrens and Samson 2011). In addition, the latent heat carried by water vapor, which is released into air during the process of condensation (vapor to liquid water) and deposition (vapor to ice), is an important source of atmospheric energy transportation and serves as the fuel for storms (Ahrens and Samson 2011). Thus, water vapor distribution plays a crucial role in the evolution of atmospheric storms and

Corresponding author e-mail: Zhizhao Liu, lszzliu@polyu.edu.hk

DOI: 10.1175/JTECH-D-16-0115.1

the vertical stability of the atmosphere (Bevis et al. 1992; Troller 2004; Ahrens and Samson 2011). Although all the intricacies that cause a precipitation event are not fully understood yet, one well-known prerequisite is that there should be enough water vapor in the atmosphere to condense onto condensation nuclei (e.g., salt and dust) to create raindrops (Ahrens and Samson 2011). Accurate measurements of water vapor distribution in spatial and temporal domains can thus contribute to determining the initiation and intensity of heavy precipitation events.

To acquire atmospheric water vapor measurements, a number of technologies, such as radiosonde and water vapor radiometer, have been developed (Niell et al. 2001; Li 2003; Ning et al. 2012; Liu et al. 2013). In recent years, global navigation satellite system (GNSS) meteorology has become a focus of research for weather analysis and forecasting due to its low operational cost, consistently high accuracy, and all-weather operability (Bevis et al. 1992; Rocken et al. 1993; Duan et al. 1996; Flores et al. 2000; Van Baelen et al. 2011; Manning et al. 2012; Brenot et al. 2013; Labbouz et al. 2013). GNSS meteorology cannot only retrieve precipitable water vapor (PWV) over individual GNSS stations (Duan et al. 1996; Elgered et al. 1997; Tregoning et al. 1998; Lee et al. 2013) but also reconstruct water vapor spatiotemporal distribution over a large area using the tomographic technique (Bender et al. 2011a; Bi et al. 2006; Brenot et al. 2014; Champollion et al. 2005; Flores et al. 2000; Jiang et al. 2014; Notarpietro et al. 2011; Rohm and Bosy 2009; Troller et al. 2006). Using a considerable number of slant wet delays (SWD) collected from a network of GNSS stations and the tomographic technique, a three-dimensional regional field of atmospheric wet refractivity can be reconstructed with a spatial resolution of several kilometers and a temporal resolution of tens of minutes (Lutz 2009; Bender et al. 2011b; Perler et al. 2011; Rohm et al. 2014). Wet refractivity is an important parameter for measuring water vapor in the atmosphere. Therefore, monitoring the spatial structure and temporal behavior of atmospheric wet refractivity has significant implication for severe weather monitoring and very short-range forecasting (Zhang et al. 2015).

Water vapor data such as wet refractivity field and PWV estimated from GNSS observations contain valuable information about the spatiotemporal variation of weather elements in meteorological event studies. Van Baelen and Penide (2009) investigated the vertical variability of water vapor during a 1-month experiment using PWV derived from three GPS stations located at various altitudes. They indicated that PWV variations in different layers could reveal the process of cloud formation before the advent of rain. Van Baelen et al. (2011) also examined the role of water vapor in precipitation life cycles and demonstrated that water vapor plays a predominant role in the evolution of precipitation. Their studies also showed a contribution of GPS tomographic results to the interpretation of convection events. Based on the statewide GPS network in Australia, Manning et al. (2012) presented a study of detecting severe weather using GPS tomography. They found that the life cycle of severe convective thunderstorms was strongly associated with the evolution of tomographic wet refractivity fields. A systematic study reported by Brenot et al. (2013) showed that GNSS tropospheric delays and horizontal delay gradients can be exploited to characterize the water vapor field during rainfall events. A significant increase followed by a decrease of tropospheric delay before a deep convective initiation was observed. Based on this finding, they successfully developed a strategy for providing the precursor to the initiation of a deep convection event. Recently, Labbouz et al. (2013) conducted a study on the leeside precipitation over mountainous regions. Analytical results indicated that low-level water vapor accumulation and convergence could be seen as precursor to the initiation of convection. Their study also demonstrated that GPS tomographic results could well reveal the moisture variation before the onset of precipitation.

Located at the coast of the South China Sea, Hong Kong, China, is a highly populated metropolis with a typical monsoon-influenced humid subtropical climate (Peel et al. 2007; Liu et al. 2014). In winter, it is affected by cool northeast monsoons that make the local weather rather cool and dry. In summer, the air over the Asian continent is warmer than that over ocean; a shallow low pressure area thus develops over the continental inland (Ahrens and Samson 2011). The pressure gradient force drives warm and moist air from ocean to the continent. As a result, Hong Kong experiences a hot and humid summer with high frequencies of heavy showers and thunderstorms. In addition, Hong Kong has undergone increased extreme precipitation events, which are likely related to the global warming and continued urbanization over the past several decades, leading to higher instabilities and unpredictability in local weather forecasting (Hong Kong Observatory 2016a). Thus, improving the capacity of forecasting extreme precipitation events in the Hong Kong region is of great significance. In this study, we use our newly developed GPS tomographic technique to detect water vapor variations during the formation, life cycle, and dissipation of heavy precipitation events. This paper is structured as follows. A detailed description of SWD

retrieval and the principle of water vapor tomography are given in section 2. Section 3 presents three case studies to investigate the relationship between the evolution of heavy precipitation and water vapor variations in Hong Kong. The conclusions and remarks are given in section 4.

2. Data and method

a. Retrieval of SWD from GPS data

As part of the atmosphere, the troposphere contains almost all of the water vapor and accounts for approximately 80% of atmospheric mass. When GNSS signals travel through the troposphere, the speed will be reduced and the direction of the rays will be deflected (Mendes 1999; Sudhir 2003). This in turn causes a delay, which is often referred to as the tropospheric delay in GNSS measurements. This tropospheric delay is composed of two parts: a hydrostatic component that is related to the total atmospheric pressure and a wet component determined by the water vapor partial pressure. Many GNSS data processing software packages, such as Bernese (Dach et al. 2007), GNSS-Inferred Positioning System (GIPSY; Webb and Zumberge 1997), GPS Analysis at Massachusetts Institute of Technology (GAMIT; Herring et al. 2010) and Positioning and Navigation Data Analyst (PANDA; Li et al. 2015) can be exploited to accurately estimate the tropospheric delay. In this study, we employ the Bernese GNSS software (Dach et al. 2007) to process the GNSS data in which the slant tropospheric delay (STD) is modeled as

$$\mathrm{STD} = (\mathrm{ZTD}_{\mathrm{apr}} + \mathrm{ZTD}_{\mathrm{est}})f(z) + \frac{\partial f}{\partial z}[G_{N,W}\cos(\phi) + G_{E,W}\sin(\phi)], \quad (1)$$

where $\mathrm{ZTD}_{\mathrm{apr}}$ (mm) is the a priori zenith tropospheric delay (ZTD), which can be calculated using an empirical tropospheric model; $\mathrm{ZTD}_{\mathrm{est}}$ (mm) is a correction to the $\mathrm{ZTD}_{\mathrm{apr}}$ that is estimated during data processing; $f(z)$ refers to the wet mapping function and the Niell mapping function (Niell 1996) is used in the Bernese software; z is the GNSS satellite zenith distance; $G_{N,W}$(mm) and $G_{E,W}$(mm) are the north and east components of the wet delay gradient, respectively; and ϕ is the satellite azimuth angle. The exploitation of the gradient can account for the anisotropy of the local troposphere, which has a nonnegligible impact on GNSS measurements, particularly at low elevations. To obtain humidity information, the slant hydrostatic delay (SHD; mm) needs to be subtracted from the STD, yielding the SWD (mm),

$$\mathrm{SWD} = \mathrm{STD} - \mathrm{SHD} + R = (\mathrm{ZTD} - \mathrm{ZHD})f(z) + \frac{\partial f}{\partial z}[G_{N,W}\cos(\phi) + G_{E,W}\sin(\phi)] + R, \quad (2)$$

where ZTD—that is, $\mathrm{ZTD}_{\mathrm{apr}} + \mathrm{ZTD}_{\mathrm{est}}$ in Eq. (1)—is directly output from the software. The zenith hydrostatic delay (ZHD; mm) can be obtained using an empirical model such as the Saastamoinen hydrostatic model (Saastamoinen 1972) with measured pressure at the surface. The R refers to the postfit residuals, which account for the errors solely due to using the gradient terms to model the anisotropic part of water vapor in the troposphere (Bi et al. 2006). The used postfit residuals are the zero-difference residuals that are extracted from the double-difference residuals output from the Bernese software by using the method proposed by Alber et al. (2000). The postfit residuals may contain unmodeled errors in GPS observations, such as the multipath noise. However, it is necessary to add the residuals, and the noise introduced into the tomography is usually below the formal uncertainty of the observations (Flores et al. 2000). To minimize the multipath effects, GPS observations with elevation angles lower than 10° are rejected in the tomography.

b. Reconstruction of wet refractivity field with tomography

Along the ray path from a receiver to a satellite, the relationship between the SWD and wet refractivity can be expressed as

$$\mathrm{SWD} = \int_l N_w \, d_l, \quad (3)$$

where N_w (mm km^{-1}) is the wet refractivity and l is the ray path (km) of the signal through the troposphere. A cutoff elevation angle of 10° is employed and the impact of ray bending can be neglected (Jiang et al. 2014). As a result, l is often regarded as a straight line in the tomography. During a period of time (e.g., 30 min), a large number of SWDs can be obtained from a ground GNSS network, such as the GPS network in Hong Kong shown in Fig. 1. These SWDs contain valuable information of water vapor and interweave in the space across different directions.

To retrieve the wet refractivity field from the GNSS-derived SWDs, the space over the network is discretized into a number of voxels and it is assumed that water vapor in each voxel is invariable and evenly distributed during a tomographic modeling period (e.g., 30 min).

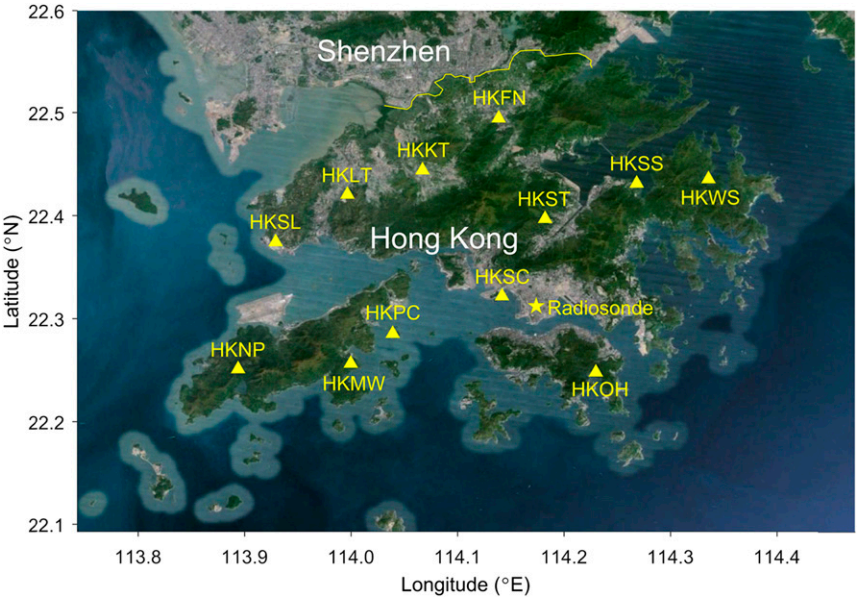

FIG. 1. Location of the 12 GPS stations (triangles) and the 1 radiosonde station (star) in Hong Kong.

After the discretization of the troposphere, each SWD can be regarded as a summation of all segments that cross through those voxels along the SWD path. Thus, Eq. (3) can be approximated by

$$\mathrm{SWD} = \sum_{i=1}^{n} N_{w_i} d_i, \tag{4}$$

where n is the number of voxels crossed by the SWD, N_{w_i} is the wet refractivity in the voxel i, and d_i (km) is the length of the ray path within the voxel i. Stacking all the SWDs in the period of tomographic modeling (30 min in this study), a linear system between the SWDs and the wet refractivity field is established,

$$\mathbf{y}_{\mathrm{SWD}} = \mathbf{A}\mathbf{x}, \tag{5}$$

where $\mathbf{y}_{\mathrm{SWD}}$ is the vector of SWD measurements, $\mathbf{A}$ is the design matrix composed of the length of the ray intercepted by each voxel, and $\mathbf{x}$ is the unknown parameter vector containing the wet refractivity of all voxels.

Because of the geometric limitation of GNSS measurements for the tomographic modeling, some of the voxels are not intercepted by any GNSS rays. Thus, the design matrix $\mathbf{A}$ is rank deficient and ill conditioned (Bender and Raabe 2007; Rohm et al. 2014). To solve this problem, pseudo-observations are usually introduced to constrain such voxels in the tomographic estimation system. In this study, two types of pseudo-observations are introduced: 1) in the horizontal domain, pseudo-observations are obtained by assuming that wet refractivity in horizontal voxels is equal to the average of its horizontal neighbors, which is a horizontal intervoxel constraint; 2) in the vertical domain, the pseudo-observations are defined as the a priori information derived from 3-day radiosonde prior to the tomographic time (Bi et al. 2006). Combining the pseudo-observations with SWD measurements, the new observation equation system becomes

$$\begin{bmatrix} \mathbf{y}_{\mathrm{SWD}} \\ \mathbf{y}_{\mathrm{r}} \\ 0 \end{bmatrix} = \begin{bmatrix} \mathbf{A} \\ \mathbf{V} \\ \mathbf{H} \end{bmatrix} \cdot \mathbf{x}, \tag{6}$$

where $\mathbf{V}$ and $\mathbf{H}$ are the coefficient vertical and horizontal intervoxel constraints, respectively; and $\mathbf{y}_r$ is the 3-day radiosonde measurements. The wet refractivity field can be estimated by least squares. Finally, the multiplicative algebraic reconstruction technique (MART) is used to improve the solution from the least squares, as described in (Chen and Liu 2014).

The Lands Department of the Government of Hong Kong Special Administrative Region (HKSAR) has been operating the Hong Kong Satellite Positioning Reference Station Network (SatRef) since 2000 (Chan and Li 2007). This network consists of 12 GPS stations and their locations are shown in Fig. 1. All the stations collect data at a 5-s sampling rate. In this study, we adopted the method developed in Chen and Liu (2014)

to perform the voxel discretization. This optimization method consists of four components: 1) top boundary determination, 2) horizontal boundary optimization, 3) vertical layer discretization, and 4) selection of optimal vertical and horizontal resolutions. The top boundary of the tomographic model is set to 8.5 km, which is derived from a statistical study of 40-yr radiosonde data, indicating the atmosphere above 8.5 km in Hong Kong can be regarded as dry air (Liu et al. 2014). The horizontal boundary optimization is achieved by moving the voxel location in latitude and longitude until the maximum number of voxels with ray crossings is reached. For the vertical layer discretization, the layer thickness increases with altitude considering the atmospheric physical property that the water vapor content decreases with the altitude. Based on extensive experiments, an optimal resolution of 0.08° (about 8.5 km) for the horizontal voxel discretization (both latitude and longitude directions) is determined (Chen and Liu 2014). In the vertical direction, from the surface to the top boundary, 15 nonuniform vertical layers are discretized (Chen and Liu 2014) with the thickness of 400 m for the bottom five layers, 500 m for the next four layers, 600 m for the next three layers, 700 m for one layer, and 1000 m for the top two layers. To characterize the dynamic water vapor variations during heavy precipitation, the water vapor tomography is performed every 30 min. For some heavy rain events, air masses will traverse a voxel very quickly (e.g., 10 min) and precipitation patterns can change very abruptly. Under this circumstance, a time resolution of 30 min may not be high enough to capture the rapid variation of water vapor. However, to obtain a reliable solution to the tomographic water vapor field determination, a period of 30 min is needed in order to get enough GNSS observations in tomographic modeling. The choice of 30 min is thus a trade-off between getting a reliable tomographic solution and getting a reasonable time resolution to characterize water vapor dynamics. The time resolution of tomography may be enhanced by densifying the GNSS network and introducing observations from other GNSS systems, such as Beidou and Galileo.

3. Evolution of water vapor during heavy precipitation events

This work will focus on the study of water vapor variation during heavy precipitation events in Hong Kong. The rainstorm warning system in Hong Kong has three warning levels, classified by the Hong Kong Observatory (HKO) according to hourly rainfall recorded or expected to fall in Hong Kong. They are, namely, Amber ($>30\,\mathrm{mm\,h^{-1}}$), Red ($>50\,\mathrm{mm\,h^{-1}}$), and Black ($>70\,\mathrm{mm\,h^{-1}}$) (Hong Kong Observatory 2016b). To study how water vapor field evolves during the life cycle of heavy precipitation events, three heavy precipitation events (each $>50\,\mathrm{mm\,h^{-1}}$) that occurred on 22 July 2010, 21 May 2013, and 30 March 2014 were selected. How the water vapor field evolves in each heavy precipitation event will be examined in the following sections. The voxel column above the HKO synoptic station (22.30°N, 114.17°E) will be used to study the vertical variation of atmospheric water vapor during the heavy rain. This is because 1) this synoptic station has recorded adequate rainfall measurements at a temporal resolution of 30 min and 2) the radiosonde station is also located within this voxel. Radiosonde can provide water vapor data for a direct comparison with the tomography. In the analysis, the total zenith wet delay (ZWD), ZWD at five altitude layers (<1000, 1000–2000, 2000–3000, 3000–5000, and >5000 m), and the relative humidity (RH) are examined to characterize the water vapor variations. ZWD of a certain layer can be derived from an integral of the tomographic wet refractivity and the vertical distance of each voxel. The RH can be calculated from

$$\mathrm{RH} = 100\frac{e}{e_s}, \tag{7}$$

where e is the water vapor partial pressure converted from the tomographic wet refractivity by

$$e = \frac{T^2 N_w}{22.9721T + 375\,463}; \tag{8}$$

and e_s is the saturation vapor pressure computed from (Ross and Elliott 1996)

$$e_s = 6.1121(1.0007 + 3.46\times10^{-6}P) \times \exp\left\{\frac{[18.729 - (T-273.15)/227.3](T-273.15)}{T-15.28}\right\}, \tag{9}$$

where P and T are the total atmospheric pressure (hPa) and temperature (Kelvin), respectively, which are provided by the numerical weather prediction model of Hong Kong (Wong 2010).

a. *Case study 1: 22 July 2010*

On 19 July 2010, Typhoon Chanthu formed as a tropical depression over the central South China Sea, about 900 km southeast of Hong Kong. It gradually moved toward the Hainan Province, China, and intensified into a typhoon early on 22 July 2010 (Hong Kong Observatory 2011). In the afternoon local time of

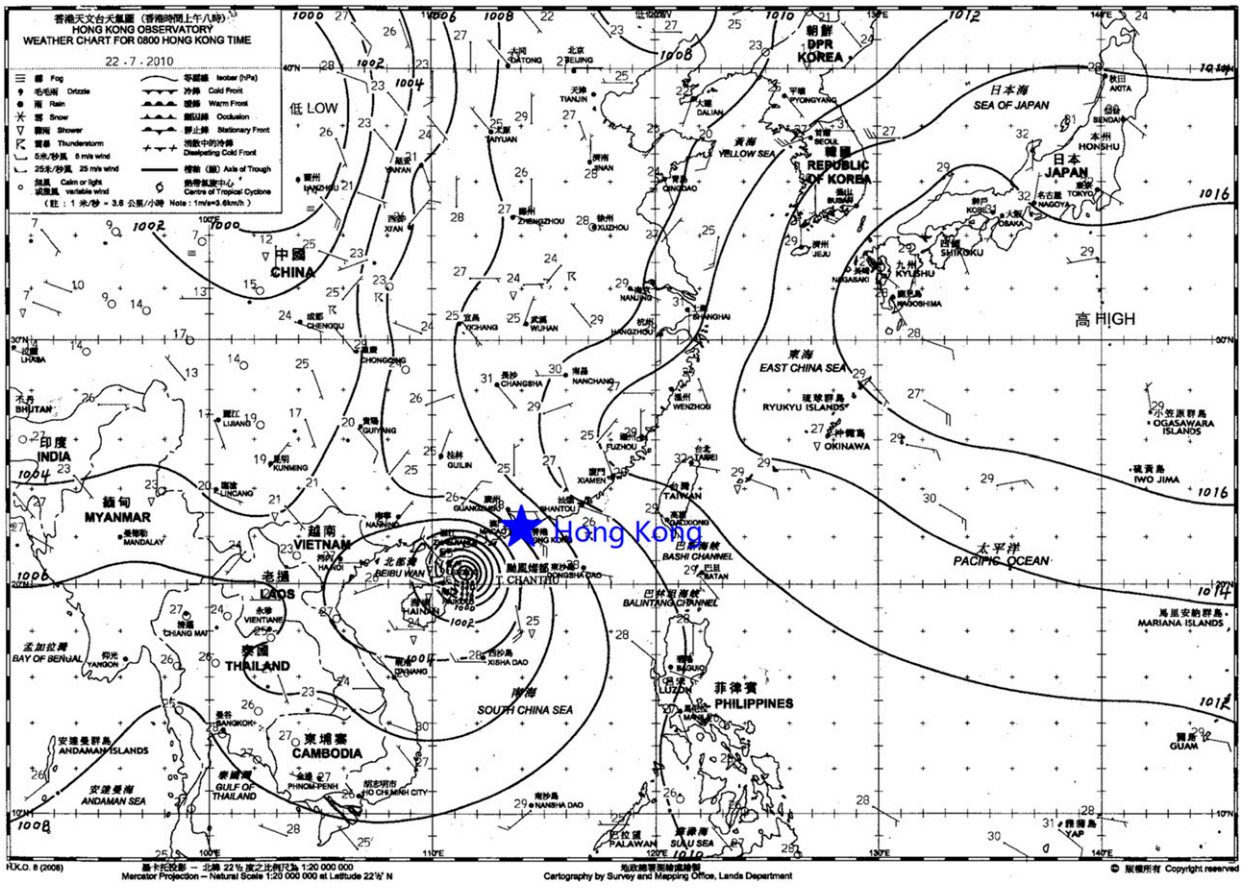

FIG. 2. Synoptic weather chart showing Typhoon Chanthu at 0000 22 Jul 2010.

this day, Chanthu made landfall in the southwest of Guangdong Province, China (see Fig. 2). It gradually weakened into a tropical depression as it moved across the Guangxi Autonomous Region on 23 July 2010. During the typhoon, at least seven casualties in Guangdong and Hong Kong were reported and more than 2900 houses were destroyed by the rainstorms. The total amount of economic losses was up to about 2.21 billion RMB (Hong Kong Observatory 2011).

Chanthu caused enormous impacts on Hong Kong though it did not directly pass through Hong Kong. The heavy rain started from 0700 UTC (hereinafter, all times are in UTC, local time = UTC + 8) and ended at 1030 22 July 2010. During the 3.5 h, a rainfall of 169 mm was recorded at the HKO synoptic station. Especially during the 2-h period from 0830 to 1030, about 150 mm of rainfall were recorded. According to the European Centre for Medium-Range Weather Forecasts (ECMWF) interim reanalysis (ERA-Interim) products (Dee et al. 2011) with a horizontal resolution of 0.5°, the meteorological synopsis over southern China at 0600 (prior to heavy rain) and 1200 (after heavy rain) 22 July 2010 is shown in Fig. 3. The geopotential height contours in black at 500 and 850 hPa indicate Chanthu over the western coastal areas of Guangdong Province. The filled contours show RH at 500 and 850 hPa. It can be seen in Figs. 3a and 3b that the air aloft at 500 and 850 hPa around Chanthu has relatively higher RH, which indicates higher water vapor content than other regions. At 1200, the typhoon moved northwestward into the Guangxi Autonomous Region (Figs. 3c and 3d). Comparing Figs. 3c and 3a, it can be observed that water vapor over the region covered by Chanthu and the Hong Kong region experienced decreases at the 500-hPa level. However, as shown in Figs. 3b and 3d, the region with high RH (>90%) extended significantly at the 850-hPa level. In the Hong Kong region, RH increased quickly from 80%–85% to 90%–95%. In addition, the wind fields are also presented with red arrows. Over Hong Kong, strong southeasterly and southerly winds with speeds of about 15–25 m s^{-1} persisted. Figure 4 shows the vertically integrated moisture flux divergences (mm day^{-1}) and the vertically integrated water vapor transport (IWT; kg m^{-1} s^{-1}) derived from ERA-Interim

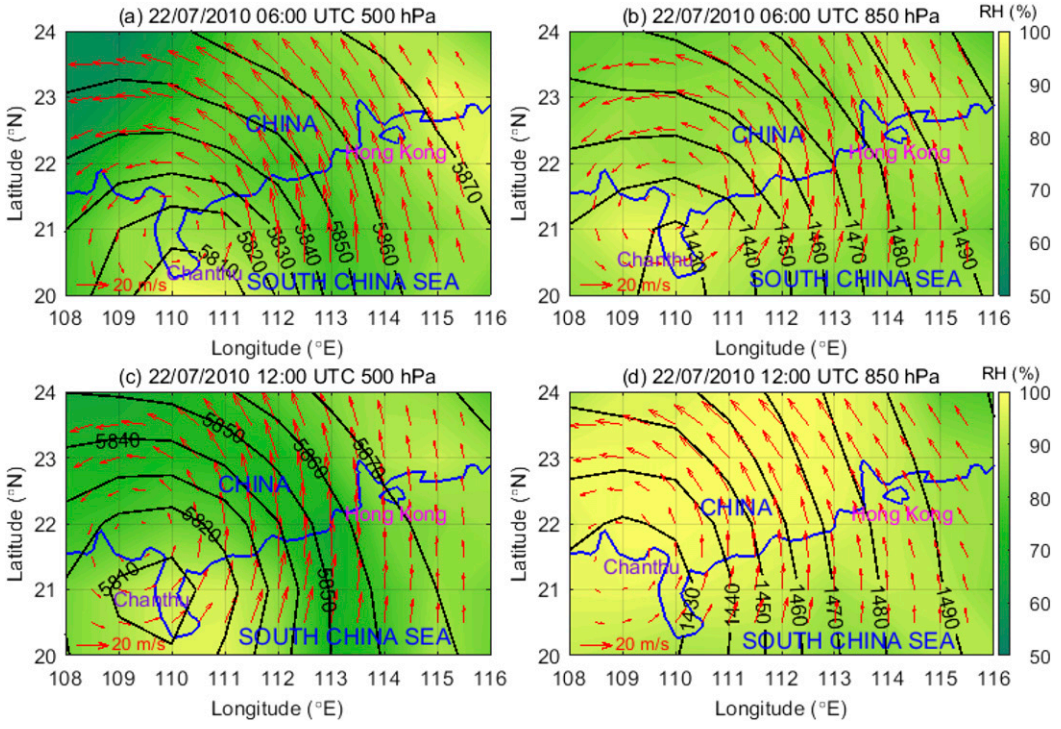

FIG. 3. Isobaric analysis at (a),(c) 500 and (b),(d) 850 hPa at 0600 and 1200 22 Jul 2010, respectively, over southern China. Black contours represent the geopotential heights (gpm). Color shading represents RH (%). Red arrows are wind vectors with the scale at bottom left in each panel. Meteorological data are derived from ERA-Interim products.

products. At 0600 UTC 22 July, 1 h before the heavy rain, high moisture convergences of 30–40 mm day^{-1} occurred over Hong Kong. A large amount of moisture from the South China Sea flowed into Hong Kong with IWT values of ~1000 kg m^{-1} s^{-1}. The magnitude of moisture convergence decreased greatly at 1200. It was Typhoon Chanthu that brought abundant warm and humid air and resulted in severe precipitation in Hong Kong.

The temporal resolution of the ECMWF data is 6 h; thus, ECMWF cannot characterize the water vapor variations during the heavy rain. To examine the water vapor evolution during this heavy precipitation event,

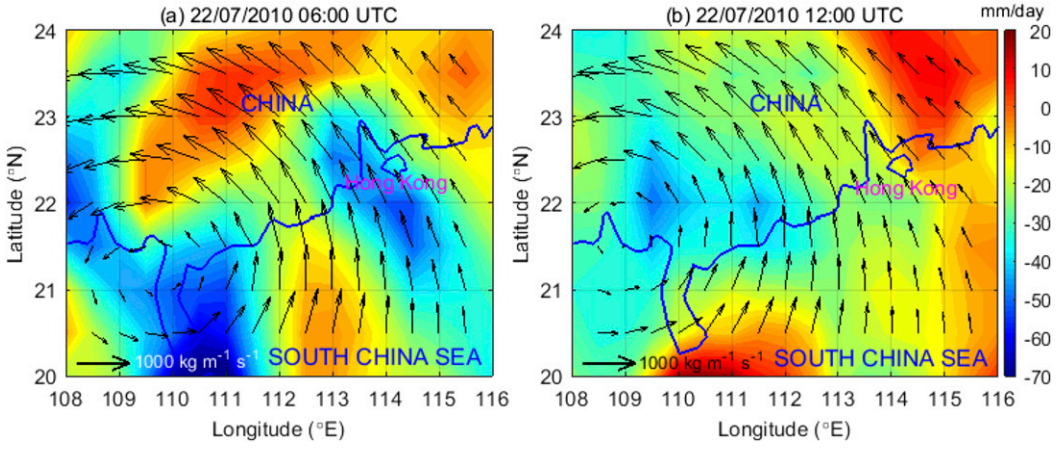

FIG. 4. Vertically integrated moisture flux divergences (mm day^{-1}) from ERA-Interim products for epochs (a) 0600 and (b) 1200 22 Jul 2010. Black arrows present IWT vectors (kg m^{-1} s^{-1}), with the scale at the bottom left of each panel.

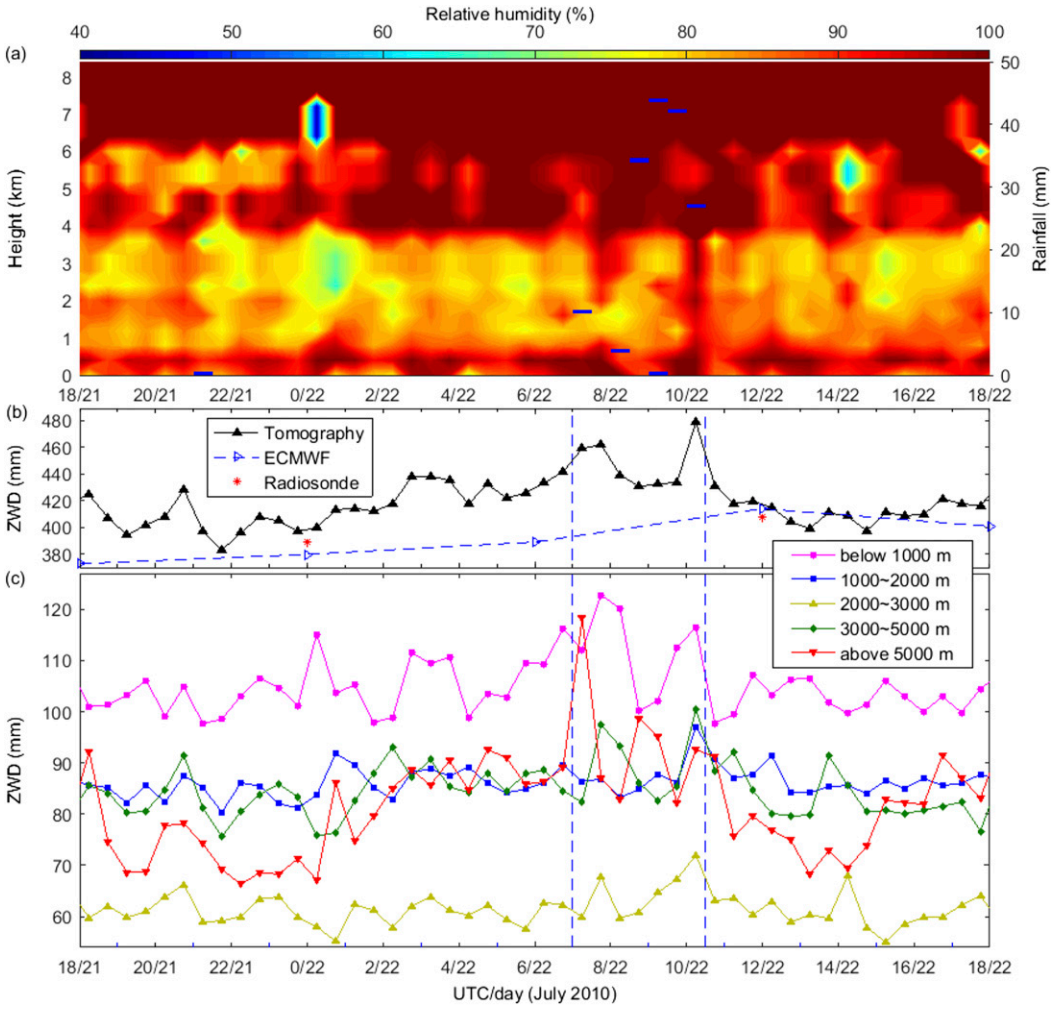

FIG. 5. Evolution of (a) tomographic RH profiles; (b) total ZWD from tomography (black), ECMWF (blue), and radiosonde measurements (red asterisks); and (c) ZWD in five layers every 30 min from 1800 21 Jul 2010 to 1800 22 Jul 2010 over the HKO synoptic station. In (a), short blue horizontal line segments show the rain gauge measured rainfall every 30 min with values on the right vertical axis.

the 3D wet refractivity field was constructed using the tomographic technique with a temporal resolution of 30 min. The RH was then converted from the wet refractivity according to Eqs. (7)–(9). SWDs retrieved from SatRef during 21–23 July 2010 are the measurements of the tomography.

Figures 5a–c show the evolution of RH profiles, total ZWD, and ZWD at five layers over the HKO synoptic station during the period from 1800 21 July to 1800 22 July 2010, respectively. Significant fluctuations are observed during the period, and the RH is very high in layers below 1000 and above 4000 m, approaching saturation. Figure 5a also shows the rainfall gauged at the HKO synoptic station with a temporal resolution of 30 min (see the blue bar). We can see that the rain started from 0700 and the heavy precipitation began at 0830 and lasted for 2 h until 1030. A more detailed illustration of the evolution of RH profiles during the heavy rain period of 0730–1100 22 July can be found in Fig. 6. Subgraphs tagged with "a" and "b" refer to the RH sections along the longitude of 114.17°E (south–north section) and latitude of 22.30°N (west–east section), respectively. Examining Fig. 5b, we can observe that the variation of the total ZWD is consistent with that of the RH. Approximately 10 h (i.e., 2200 21 July) prior to the precipitation event, the total ZWD began to increase from about 380 to around 460 mm at 0800 22 July, then it underwent a quick decrease to 430 mm by 0900 22 July, followed by a slight increase. Around 1000, it suddenly increased to 479 mm and then dropped quickly to 417 mm at 1100. Figure 6 captures more details of this variation. In Figs. 6a, 6b, 7a, and 7b, we can

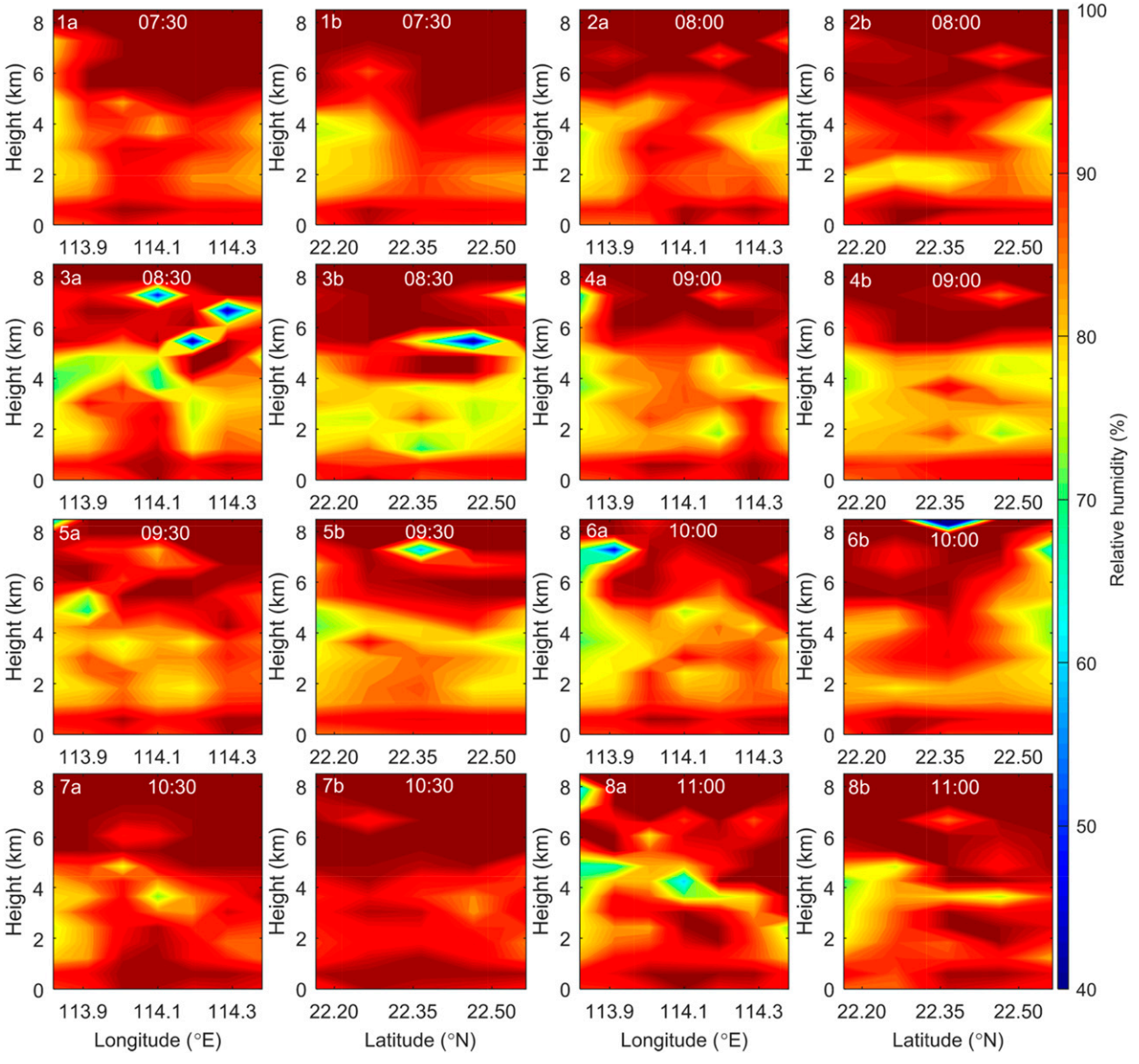

FIG. 6. (top left to bottom right) Evolution of tomographic RH profiles (%) every 30 min from 0730 to 1100 22 Jul 2010. Panels tagged with an a(b) refer to the RH sections along the longitude of 114.17°E (the latitude of 22.30°N).

observe a significant increase in RH at various heights, which is likely associated with the inflow of moisture. Afterward, in Figs. 8a and 8b, water vapor depletion possibly due to the generation of hydrometeors is clearly seen at altitudes between 4000 and 6000 m. Generally, the total ZWD increased prior to precipitation and decreased during the pouring rain. The total ZWD derived from the ECMWF, presented in Fig. 5b (dashed lines with hollow signs), shows a trend similar to the tomographic ZWD, though large differences exist at epochs of 1800 21 July and 0600 22 July. The large discrepancies are probably due to the unsatisfactory performance of ECMWF, especially at epochs when no radiosonde observations are available for the data assimilation. For epochs when radiosonde data (asterisks) were available, as seen in Fig. 5b, the three kinds of observations show a good agreement. As mentioned before, the average measurement of radiosondes during the 3 days prior to the tomographic time is used to constrain the vertical voxels. Radiosonde observations made at the tomographic time are not involved in tomography. Therefore, radiosonde can be seen as independent measurements to assess the tomographic solutions, and their good agreement demonstrates the high performance of tomography.

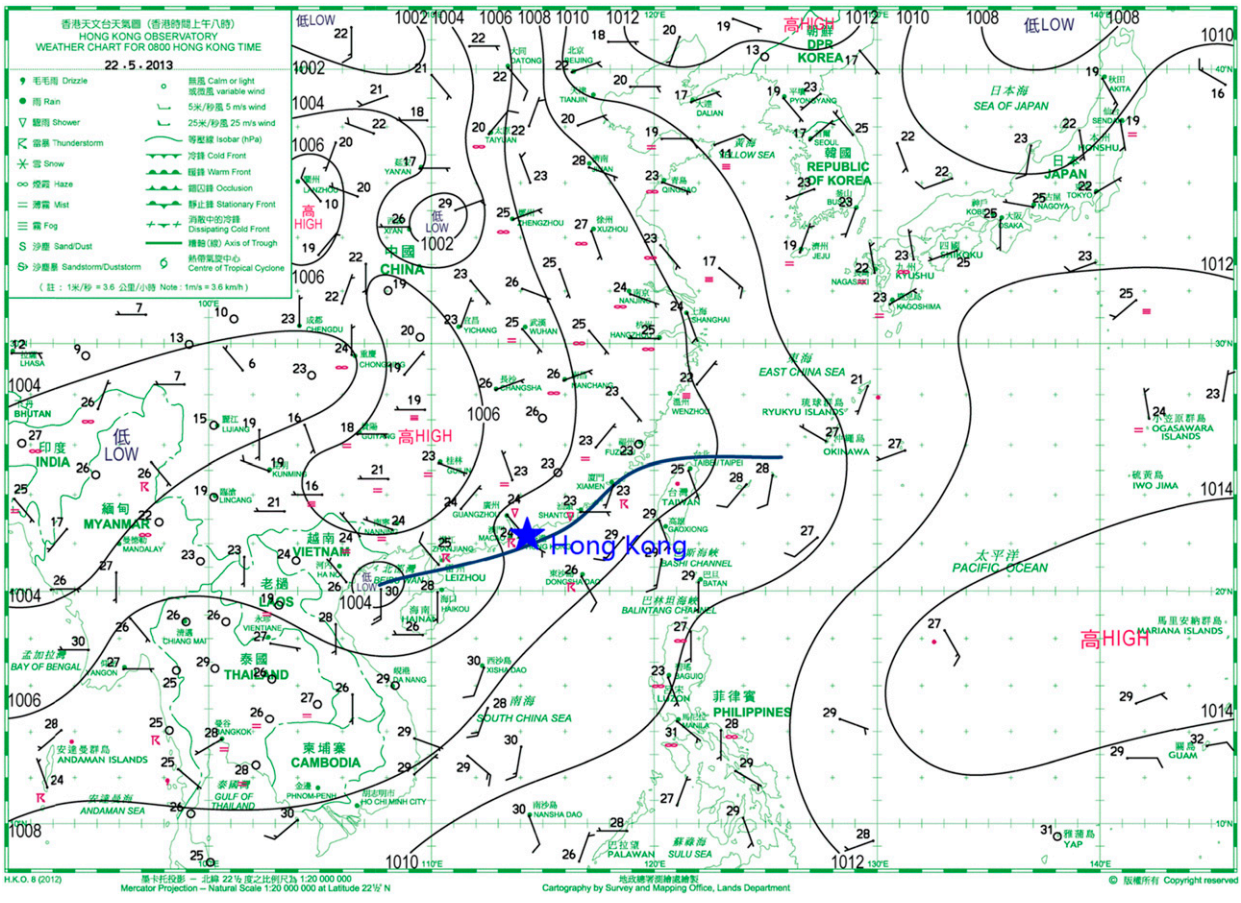

FIG. 7. Synoptic weather chart at 0000 22 May 2013.

Figure 5c presents the tomographic ZWD at five vertical layers, but the ECMWF and radiosonde cannot show such vertical variations with time due to their relatively low temporal resolution. It can be observed that a large ZWD variation with time mainly occurred above the altitude 3000 m, referring to the green and red lines. This is clearly shown in Fig. 6, as large RH disturbances mainly occurred at altitudes above 3000 m. As seen in Fig. 5c, 2 h prior to the rain (i.e., 0500 22 July), ZWDs below the altitude of 1000 m (the pink lines) showed an evident increase, while ZWDs in the other four layers are characterized as fluctuations. From 0200 to 0730, ZWDs above 5000 m (the red lines) increased significantly from ~80 to ~120 mm, which is probably due to a massive amount of water vapor flowing into the upper air over Hong Kong, as suggested by Figs. 3 and 4. It is interesting to see from Fig. 5c that water vapor below 5000 m decreased slightly during the period from 0700 to 0730. However, water vapor above 5000 m at this moment showed a remarkable increase. Within the 30 min from 0730 to 0800, the ZWD above 5000 m dropped quickly, while the ZWD below 5000 m showed an evident increase. This phenomenon also occurred during the period 0800–1000, when the rain was heavy. The ZWD above 5000 m also experienced a strong increase, followed by a quick decrease and vice versa for the ZWD below 5000 m. This phenomenon may be due to the inflow of humid air from Typhoon Chanthu to Hong Kong. And then the water vapor aloft condensed into raindrops and sank into the lower layers, while some of them evaporated again with the temperature increase. This speculation can be supported by Fig. 6 to some extent. From Figs. 4a and 4b to 5a and 5b, RHs above 6000 m decreased obviously, while high RH (>85%) regions spread below 6000 m. This process implies the creation of raindrops through water vapor condensation. After the heavy rain event, the water vapor above 3000 m decreased quickly, while water vapor below 3000 m did not show any decrease.

b. Case study 2: 21 May 2013

On 21 May 2013, influenced by a trough of low pressure lingering over the coast of Guangdong Province (see Fig. 7), Hong Kong suffered several torrential rains,

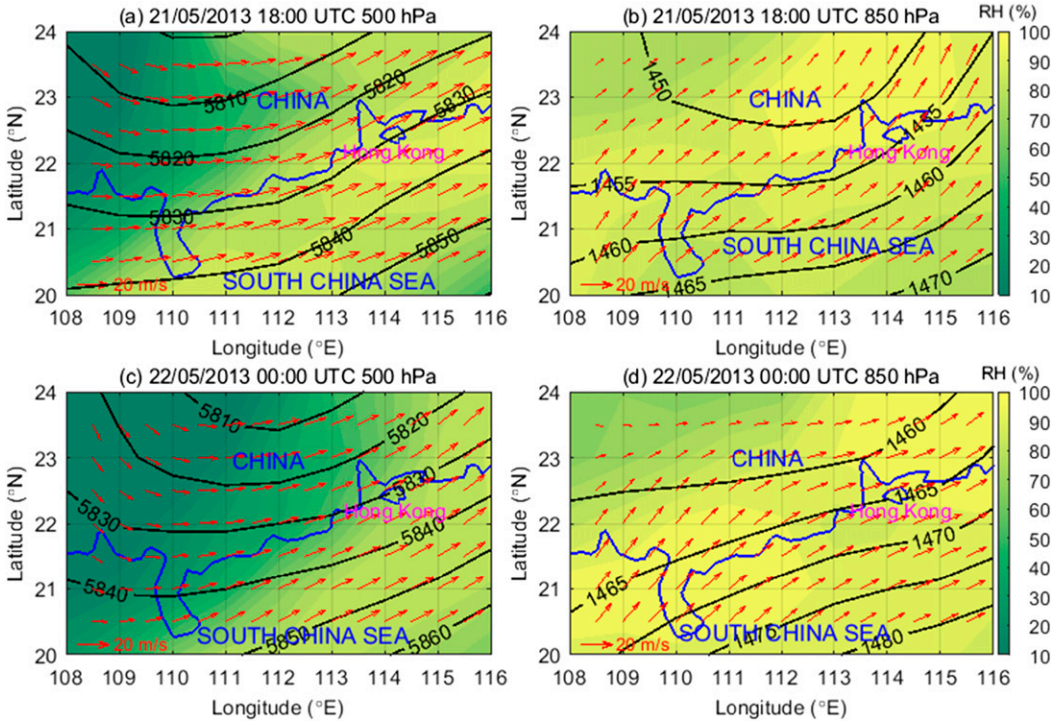

FIG. 8. As in Fig. 3, but for 1800 21 May and 0000 22 May 2013.

which caused major floods and massive landslides in some places. During the period from 1600 21 May to 0600 22 May 2013, the HKO synoptic station gauged a rainfall of 190 mm. During 1930–2030, very heavy precipitation of 102 mm was recorded and HKO issued the first Black Rainstorm Warning of 2013. Figure 8 presents the meteorological synopsis over southern China at 1800 21 May and at 0000 22 May at two pressure levels: 500 and 850 hPa. It can be observed that the air over Hong Kong and the surrounding regions was very humid. Water vapor over Hong Kong decreased slightly at both pressure levels within the 6 h from 1800 21 May to 0000 22 May. The wind field information showed that strong southwesterly winds occurred over Hong Kong. Combined with the moisture flux divergences and IWT fields presented in Fig. 9, it is clear that the strong winds brought water vapor from the southwest to Hong Kong.

The tomographic technique provides a potent tool for investigating water vapor spatiotemporal variation for the development, evolution, and dissipation of this severe

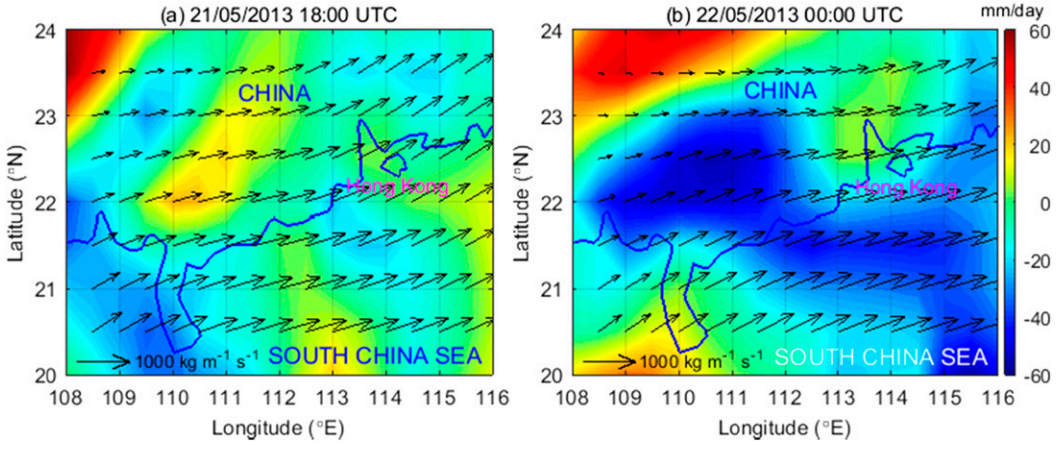

FIG. 9. As in Fig. 4, but for (a) 1800 21 May and (b) 0000 22 May 2013.

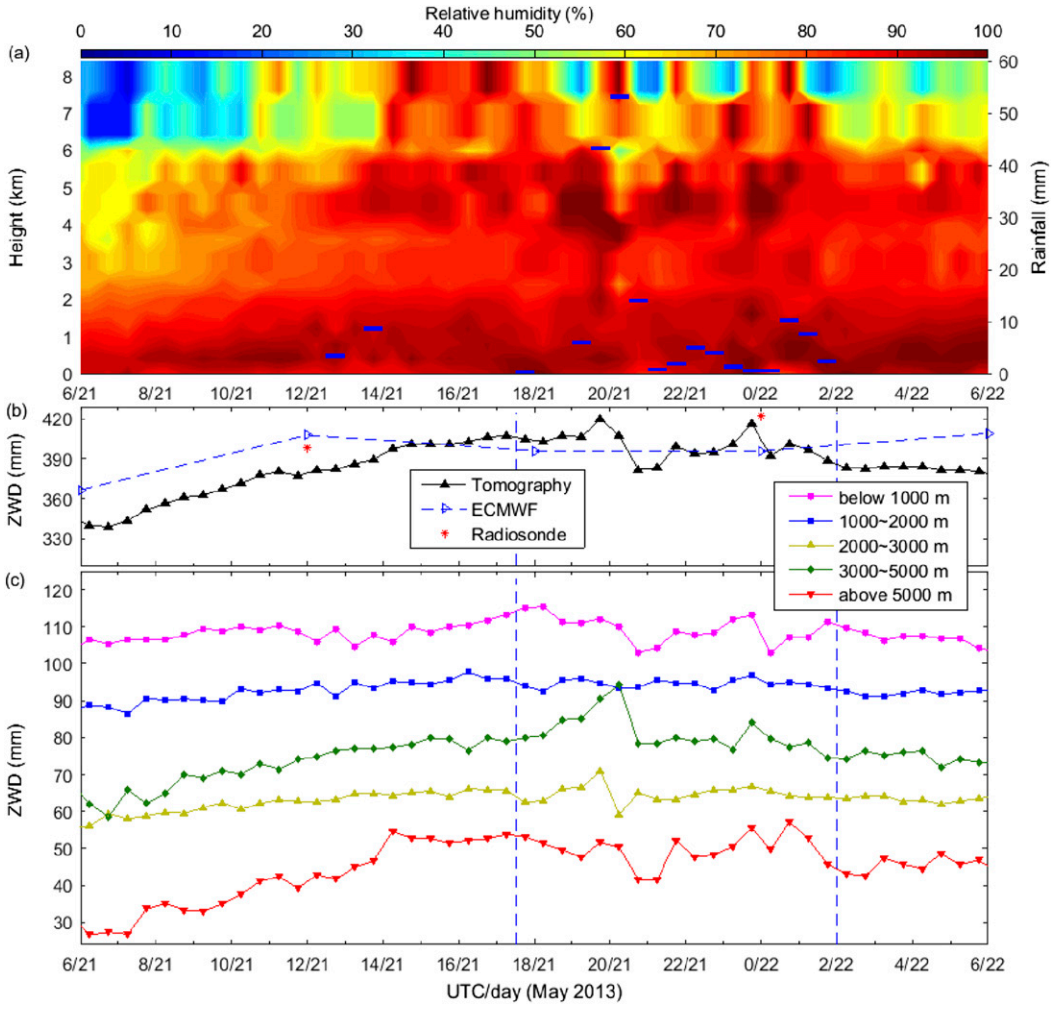

FIG. 10. As in Fig. 5, but for 0600 21 May to 0600 22 May 2013.

precipitation event. In Fig. 10a, the focus is on the precipitation event beginning at 1730 21 May, and the torrential rain started 2 h later and lasted 1.5 h, 1930–2100.

In Fig. 10b, we can see that preceding the heavy precipitation, the total ZWD continuously increased from 340 mm at 0700 21 May to 420 mm by 1930. At the peak time (1930), torrential rain occurred, followed by a quick decrease of the total ZWD. Within 5 h following 2100, the total ZWD fluctuated, while the heavy rain weakened to drizzle, and it decreased quickly after the end of precipitation (0200 22 May). As shown in Fig. 10b, the tomographic ZWDs were well validated by the radiosonde-measured ones. The trend of the total ZWD derived from ECMWF generally agreed with the tomographic results. Figure 10c depicts ZWD time series at five vertical layers. During the 10 h before the rain started at 1730 21 May, water vapor above 3000 m increased greatly with respect to that below 3000 m. In the layer below 1000 m, as shown in Fig. 10c, the ZWD reached the maximum at 1800, when the rain just began. Unlike the total ZWD, the ZWD below 1000 m stopped increasing and decreased quickly during the pouring rain. ZWDs between 1000–2000 m kept steady. The total ZWD increased during 1800–2000 21 May mainly in the layers between 2000–5000 m. Water vapor above 5000 m showed a slow decrease followed by a sudden increase during 1800–2000 21 May. The ZWD decreased during the heavy rain could be explained as follows: a considerable amount of water vapor condensed into water droplets that are not interactive with GPS signals. For a closer examination during the heavy rain, as shown in Figs. 11(2a), (2b), (3a), (3b), (4a), and (4b), an evident RH decrease can be observed in most altitudes as bluish and yellowish regions expanded. This variation indicates the generation of raindrops through condensation, and perhaps also linked with the washing of the

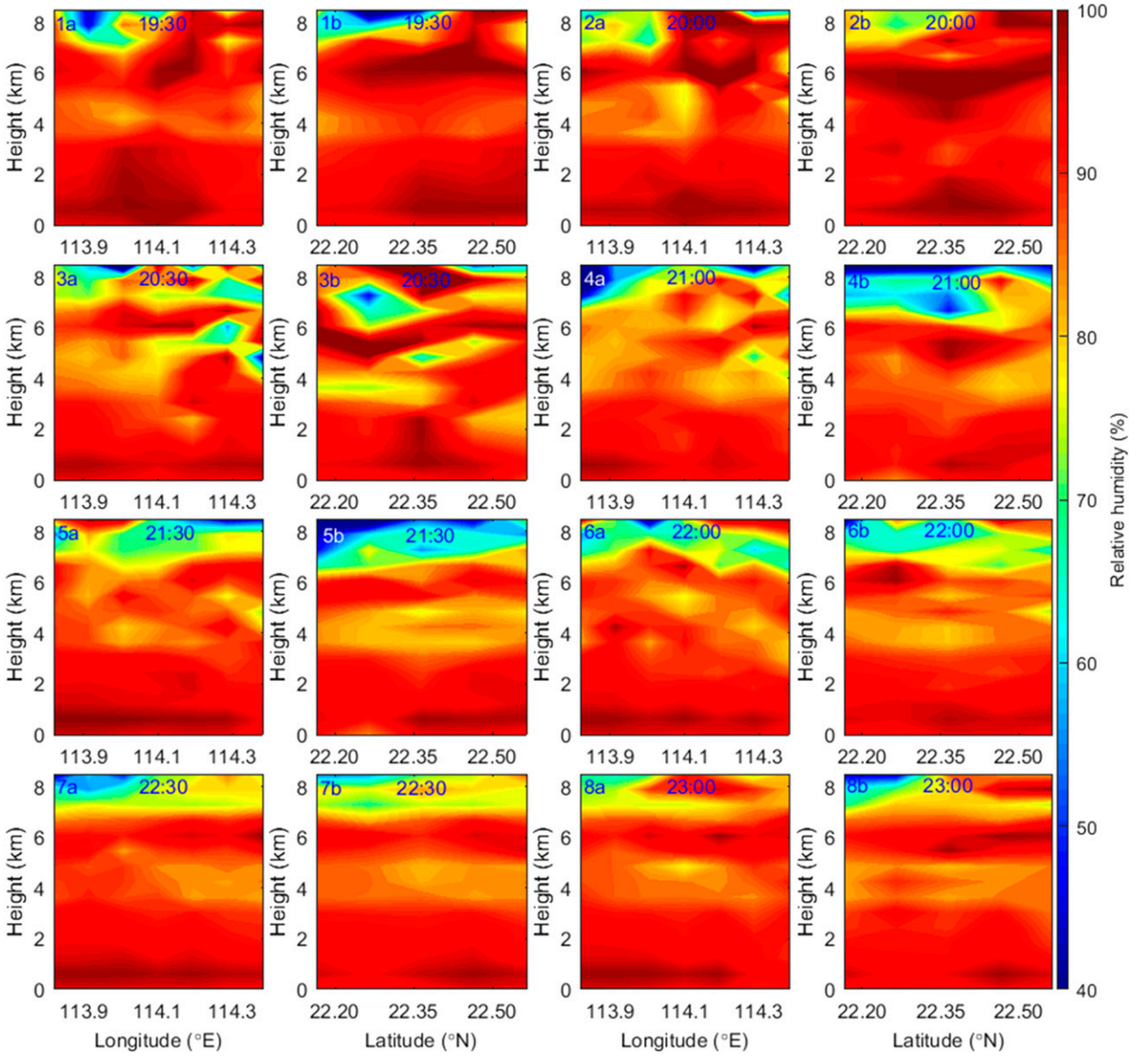

FIG. 11. As in Fig. 6, but from 1930 to 2300 21 May 2013.

lower atmosphere while pouring rain. In the subsequent 5 h (from 2100 21 May to 0100 22 May) after the heavy precipitation, light rain continued and water vapor in different layers still showed a number of fluctuations. This indicated that the atmosphere was in an unstable condition and precipitation continued to occur. Once the precipitation stopped, it could be found from Fig. 10c, 0200–0600 22 May, that water vapor in different layers gradually decreased toward a steady state.

c. *Case study 3: 30 March 2014*

At the end of March 2014, an active trough of low pressure (Fig. 12) dominated southern China and brought several episodes of heavy rains and intense thunderstorms to Guangdong Province. Figure 13 shows the meteorological synopsis over southern China at 1200 and 1800 30 March 2014. Figures 13a and 13c show that the air at the 500-hPa level over the Hong Kong region was dry and that very strong westerly winds persisted. However, at the 850-hPa level the region was covered by warm, moist air and dominated by strong southwesterly winds. Figure 14a shows that large moisture convergence occurred north of Hong Kong and Hong Kong had moisture flux convergence of 20–30 mm day^{-1} at 1200. The low-level wind transported the moisture from the southwest to Hong Kong with IWT values of ~900 kg m^{-1} s^{-1}. In Fig. 14b, 3 h after the heavy rain, large moisture divergences occurred in Hong Kong. On

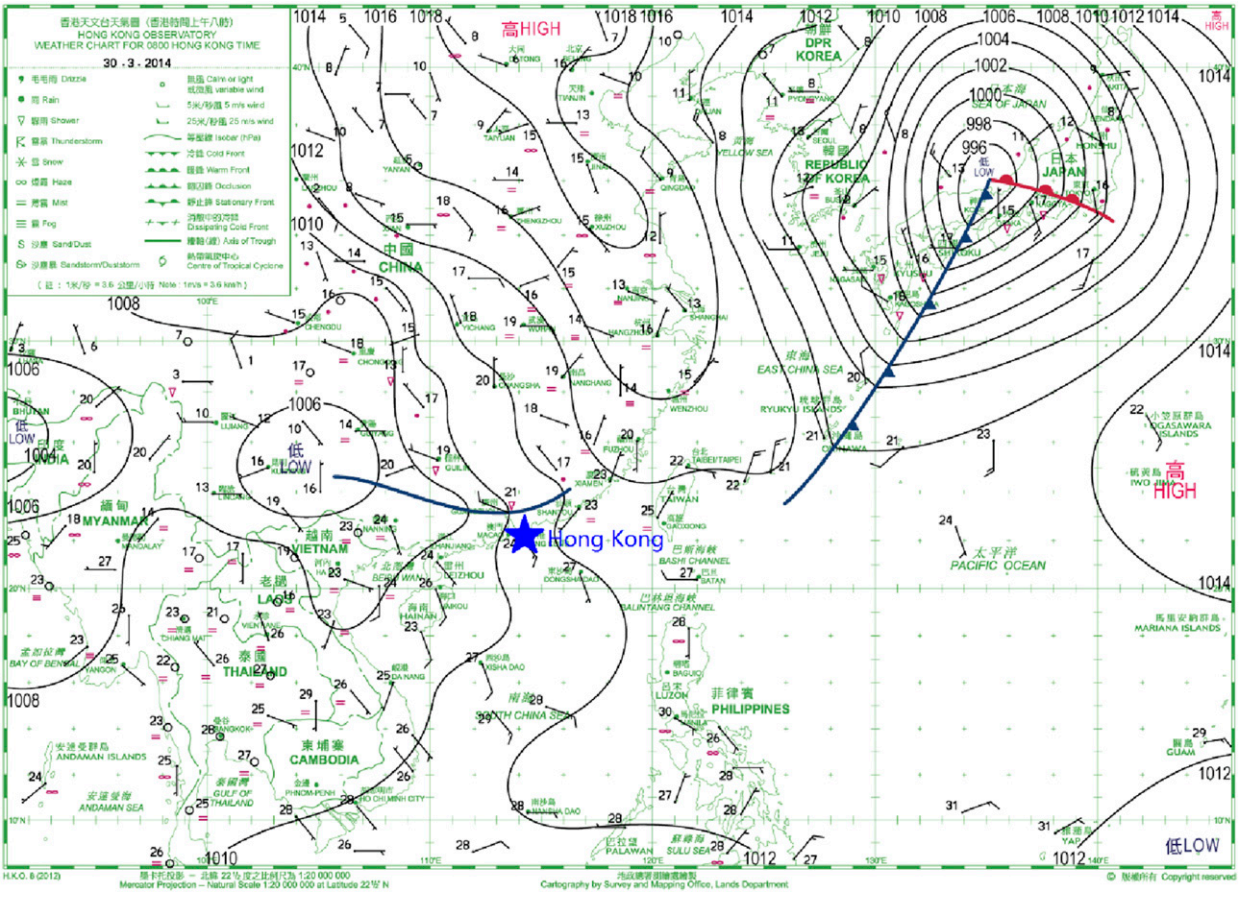

FIG. 12. Synoptic weather chart at 0000 30 Mar 2014.

this day, heavy precipitation and widespread hails lashed Hong Kong. Over a period of 3–4 h, more than 100 mm of rainfall were recorded in most areas of Hong Kong. A Black Rainstorm Warning was issued at 1240. This was the first time HKO issued a Black Rainstorm Warning for a month of March since the Rainstorm Warning System was officially introduced in 1992. During 1300–1400, the HKO synoptic station measured an hourly rainfall of 56 mm, which set the highest record for a month of March since 1884. The abrupt heavy precipitation event resulted in many flash flood events in Hong Kong and caused significant economic losses.

Figure 15 shows the evolution of water vapor during the period from 0600 29 March to 0000 31 March. The two vertical blue lines in Figs. 15b and 15c indicate the heavy rain that occurred between 1100–1500 30 March. As shown in Fig. 15b, tomographic ZWDs basically agreed well with those measured by radiosonde. Large discrepancies between tomography and ECMWF occurred at epochs of 0600, 1200, and 1800 30 March, which are most likely because ECMWF was unable to reproduce the large variations of water vapor at high layers (above 5000 m) during the heavy rain. We can see the total ZWD increased from about 290 mm at the initial time 0000 30 March to about 330 mm within 10 h. During this heavy precipitation event, the total ZWD quickly increased, followed by a rapid decrease. Then, it began to decrease until the precipitation stopped at 1500 30 March, which was similar to the other two events described in the abovementioned sections. Examining Fig. 15c, it is interesting to see that water vapor above 5000 m experienced very sharp fluctuations during 1200–1500 30 March. Ten hours prior to the heavy rain (0000–0200 30 March), ZWDs above 5000 m lingered around 20 mm. They reached about 120 mm at around 1330 during the heavy precipitation event. A better visual description of RH variation is provided in Fig. 16. Delicate increases and decreases in RH, which are related to water vapor accumulation and depletion, respectively, can be observed. As shown in the plots labeled 3a, 3b, 4a, 4b, 5a, and 5b in Fig. 16, not all the regions above 5000 m experienced remarkable water vapor increases during 1230–1330, while obvious RH decreases occurred in some sections. This reveals a

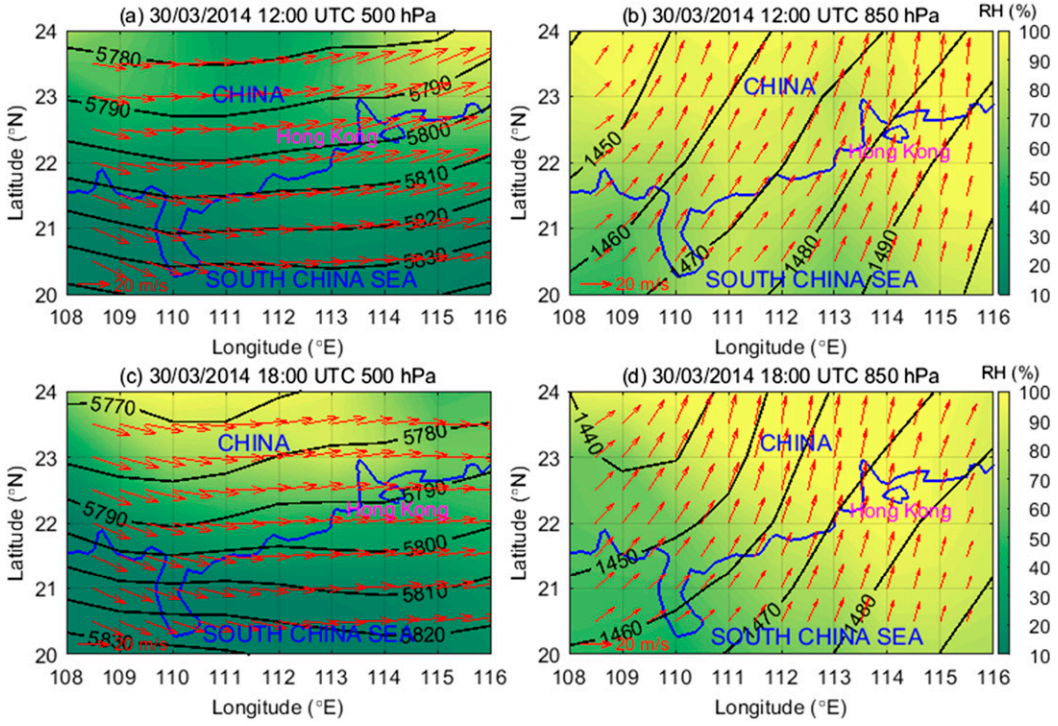

FIG. 13. As in Fig. 3, but at 1200 and 1800 30 Mar 2014.

rather unstable atmospheric condition during the pouring rain, and the observed quick ZWD increase above 5000 m over the HKO synoptic station was very likely due to moisture inflow from other places. In addition, in Fig. 15c, ZWD between 3000 and 5000 m also displayed great variations. During the period 1200–1330 30 March, the ZWD above 5000 m increased remarkably from 45 to 118 mm, while the ZWD below 5000 m underwent a decrease–increase–decrease process. As revealed in Fig. 15a, the air above 5000 m was saturated during the heavy rain, providing abundant water for the heavy precipitation. When the ZWD above 5000 m reached the maximum, a severe rain occurred with a rainfall of about 48 mm per 30 min. With the heavy rain pouring, the ZWD decreased rapidly. The southwesterly flow at 850 hPa shown by the reanalysis data at 1200 in Fig. 13a depicted a high moisture area passed over the inland area associated with the perturbed westerly flow at 500 hPa. Strong southwesterly moisture transport over Hong Kong can be observed in Fig. 14. The mesoscale

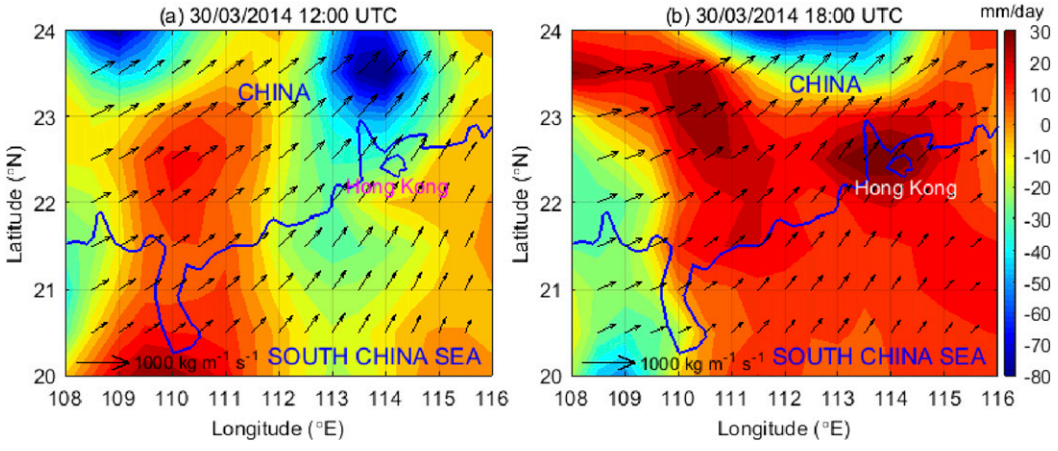

FIG. 14. As in Fig. 4, but for (a) 1200 and (b) 1800 30 Mar 2014.

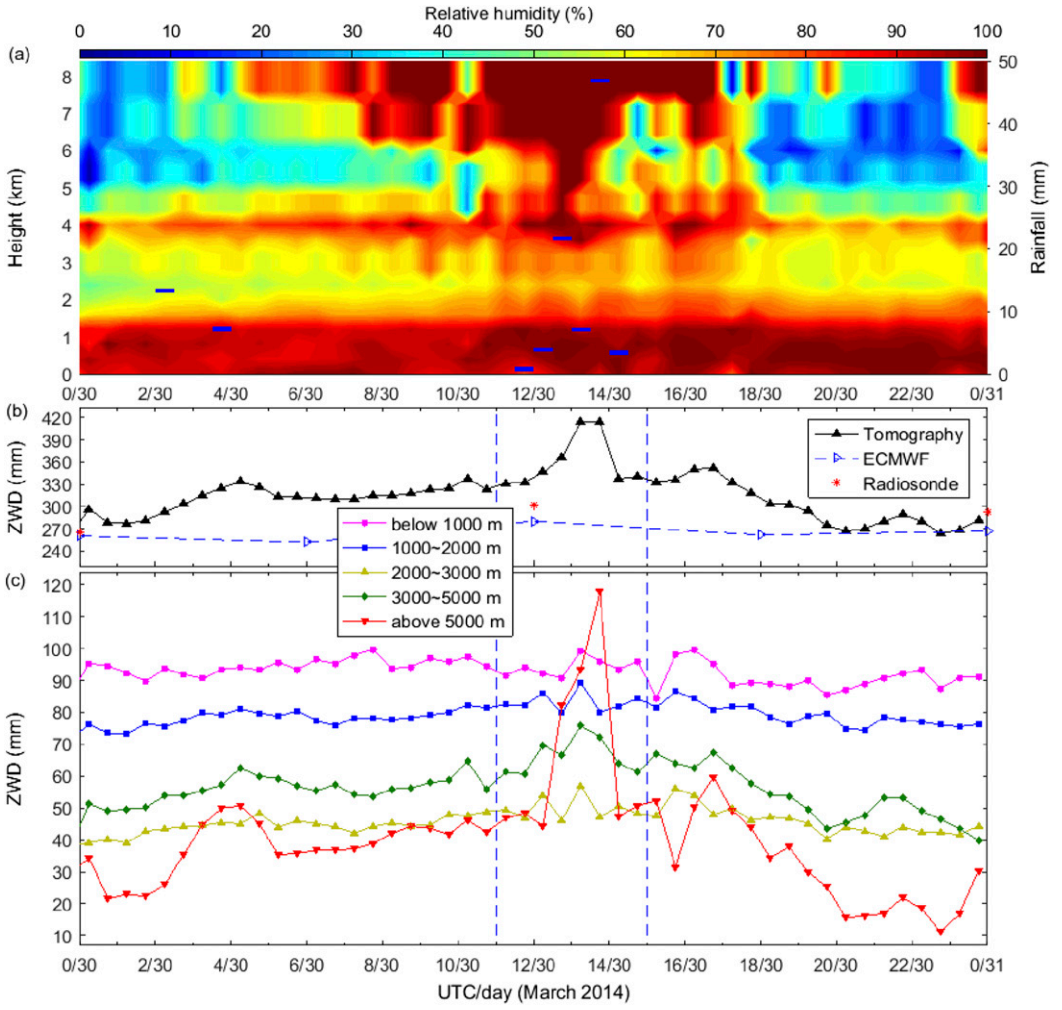

FIG. 15. As in Fig. 5, but from 0000 30 Mar to 0000 31 Mar 2014.

development of a storm environment over the coastal areas of Guangdong Province was supported by the increase in local water vapor as revealed from the GPS tomography data.

4. Discussion and conclusions

Water vapor plays a critical role in the development of severe weather events such as heavy precipitation. Accurate information of water vapor distribution has significant implications in the detection of atmospheric stability and forecasting of the evolution of severe weather events. Water vapor tomography has been demonstrated to be a powerful technique for retrieving highly dynamic water vapor distribution in both space and time domains. It has been demonstrated that it is possible to monitor the evolution of water vapor during the development, evolution, and dissipation stages of a severe weather event.

This paper studied the evolution of water vapor during three heavy precipitation events that occurred in Hong Kong on 22 July 2010, 21 May 2013, and 30 March 2014. All the three events recorded hourly rainfall exceeding 50 mm. Using the SWDs derived from the Hong Kong GPS network, 3D atmospheric wet refractivity fields were tomographically reconstructed for these heavy precipitation events. The total ZWDs over the HKO synoptic station as well as the ZWDs at five altitude layers (<1000, 1000–2000, 2000–3000, 3000–5000, and >5000 m) were derived from the tomographic results. They were compared with the moisture contents and convergence diagnosed from the ERA-Interim data. The water vapor variations detected by the tomography were validated by the ECMWF and radiosonde in Hong Kong.

From the analysis of water vapor variability during the three heavy precipitation events, several conclusions can be drawn as follows. First of all, the total ZWD in all

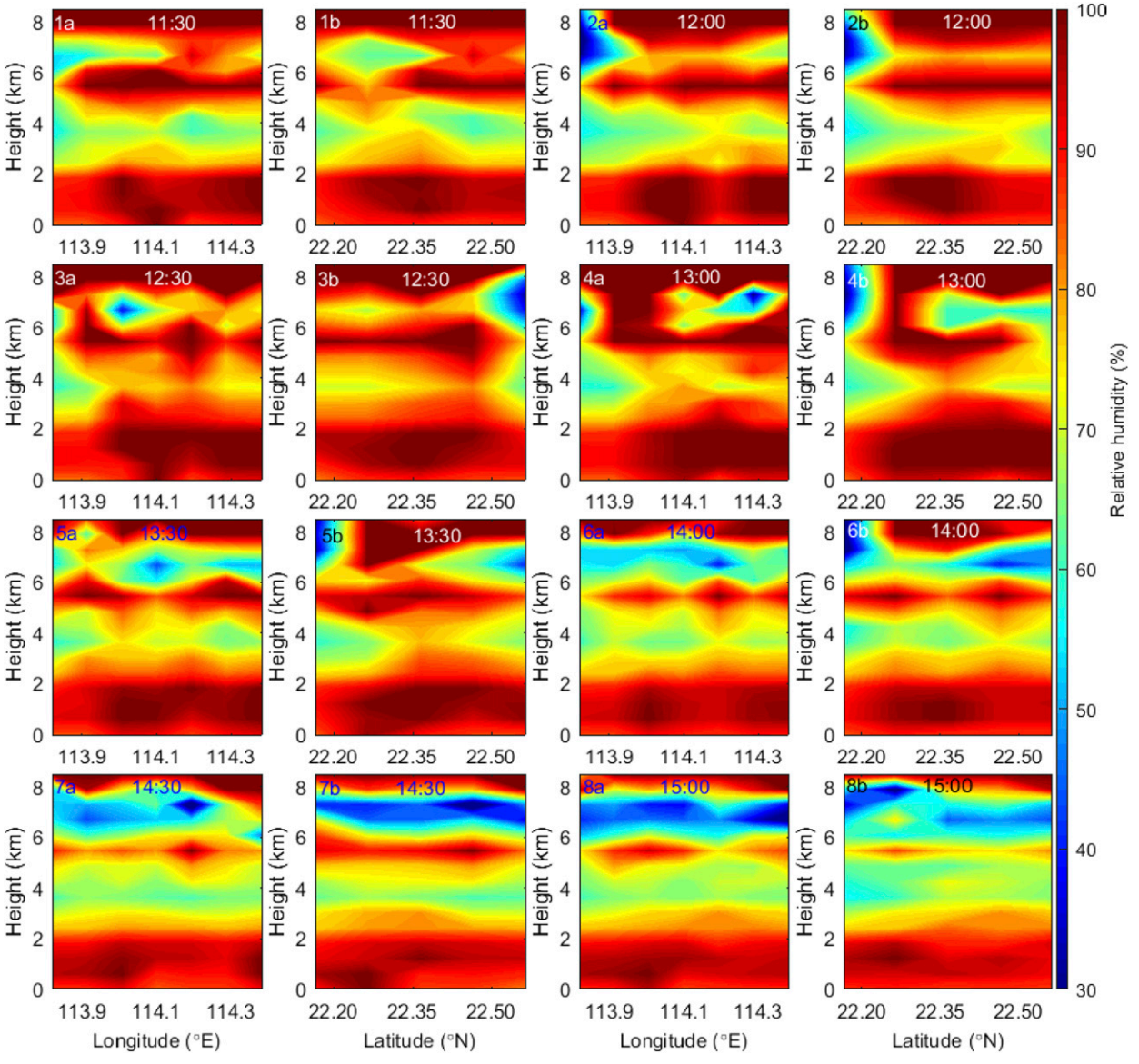

FIG. 16. Evolution of tomographic RH profiles every 30 min from 1130 to 1500 30 Mar 2014. Plots labeled with "a" refer to RH sections along the longitude of 114.17°E. Plots labeled with "b" refer to the RH sections along the latitude of 22.30°N.

three events exceeded 400 mm prior to the commencement of heavy rain. In addition, although the amount of water vapor above 3000 m accounts for only 10%–25% of the total water vapor in Hong Kong (Liu et al. 2014), it shows larger variations than that below 3000 m during heavy precipitation events. The fluctuations in the total ZWD are largely attributed to the water vapor variations in the layers above 3000 m. In the 22 July 2010 and 30 March 2014 events, we observed that the ZWD above 5000 m approached an amount of 120 mm prior to the heavy precipitation. In the 21 May 2013 event, the ZWD in the layer at 3000–5000 m experienced a significant increase with its maximum reaching 95 mm. It is also notable that water vapor in the layer at 1000–3000 m generally remained stable and did not fluctuate as much as those below 1000 or above 3000 m. The remarkable water vapor fluctuations in the altitude layers above 3000 m can be seen as precursors to heavy precipitation.

The work has demonstrated the capability of using the tomographic technique to monitor atmospheric water vapor with a high spatiotemporal resolution, through reconstructed wet refractivity fields. With additional pressure and temperature information, wet refractivity can be converted to RH. The variations of RH fields can reveal water vapor accumulation, saturation,

and condensation. By monitoring water vapor variations at different altitude layers, it is possible to reveal water vapor motions among different layers and thus to detect atmospheric stability. The characteristics of water vapor variations at different altitude layers can be exploited to detect many atmospheric processes. This study presents several positive findings from tomographic results that can be an important meteorological data source for detecting heavy precipitation events.

Acknowledgments. Zhizhao Liu acknowledges support from the Hong Kong Research Grants Council (RGC) projects [PolyU 5325/12E (F-PP0F)], the National Natural Science Foundation of China (41274039), and the Hong Kong Polytechnic University project (PolyU 152168/15E, G-YBM3). The Lands Department of the Hong Kong Special Administrative Region is thanked for providing the SatRef GPS data, and the Cartography and Cadastre Bureau (DSCC) of Macao Government of Special Administrative Region is also thanked for sharing GPS data. We also thank the Department of Atmospheric Science of the University of Wyoming for providing Hong Kong radiosonde data. Finally, the authors want to thank Mr. P. W. Chan, Mr. Sai Tick Chan, and Mr. T. L. Cheng from the Hong Kong Observatory for providing rainfall data.

REFERENCES

Ahrens, C. D., and P. J. Samson, 2011: *Extreme Weather and Climate*. 1st ed. Brooks Cole, 508 pp.

Alber, C., R. Ware, C. Rocken, and J. Braun, 2000: Obtaining single path phase delays from GPS double differences. *Geophys. Res. Lett.*, **27**, 2661–2664, doi:10.1029/2000GL011525.

Bender, M., and A. Raabe, 2007: Preconditions to ground based GPS water vapour tomography. *Ann. Geophys.*, **25**, 1727–1734, doi:10.5194/angeo-25-1727-2007.

——, G. Dick, M. Ge, Z. Deng, J. Wickert, H.-G. Kahle, A. Raabe, and G. Tetzlaff, 2011a: Development of a GNSS water vapour tomography system using algebraic reconstruction techniques. *Adv. Space Res.*, **47**, 1704–1720, doi:10.1016/j.asr.2010.05.034.

——, R. Stosius, F. Zus, G. Dick, J. Wickert, and A. Raabe, 2011b: GNSS water vapour tomography—Expected improvements by combining GPS, GLONASS and Galileo observations. *Adv. Space Res.*, **47**, 886–897, doi:10.1016/j.asr.2010.09.011.

Bevis, M., S. Businger, T. A. Herring, C. Rocken, R. A. Anthes, and R. H. Ware, 1992: GPS meteorology: Remote sensing of atmospheric water vapor using the global positioning system. *J. Geophys. Res.*, **97**, 15 787–15 801, doi:10.1029/92JD01517.

Bi, Y., J. Mao, and C. Li, 2006: Preliminary results of 4-D water vapor tomography in the troposphere using GPS. *Adv. Atmos. Sci.*, **23**, 551–560, doi:10.1007/s00376-006-0551-y.

Brenot, H., and Coauthors, 2013: Preliminary signs of the initiation of deep convection by GNSS. *Atmos. Chem. Phys.*, **13**, 5425–5449, doi:10.5194/acp-13-5425-2013.

——, and Coauthors, 2014: A GPS network for tropospheric tomography in the framework of the Mediterranean hydrometeorological observatory Cévennes-Vivarais (southeastern France). *Atmos. Meas. Tech.*, **7**, 553–578, doi:10.5194/amt-7-553-2014.

Champollion, C., F. Masson, M.-N. Bouin, A. Walpersdorf, E. Doerflinger, O. Bock, and J. Van Baelen, 2005: GPS water vapour tomography: Preliminary results from the ESCOMPTE field experiment. *Atmos. Res.*, **74**, 253–274, doi:10.1016/j.atmosres.2004.04.003.

Chan, K.-K., and C. Li, 2007: The Hong Kong Satellite Positioning Reference Station Network (SatRef)—System configurations, applications and services. *Proc. FIG Working Week 2007: Strategic Integration of Surveying Services*, Hong Kong Institute of Surveyors/International Federation of Surveyors, Hong Kong, China, 13 pp. [Available online at http://www.fig.net/resources/proceedings/fig_proceedings/fig2007/papers/ts_5a/ts05a_04_chan_li_1332.pdf.]

Chang, N.-B., and D.-H. Guo, 2006: Urban flash flood monitoring, mapping and forecasting via a tailored sensor network system. *2006 IEEE International Conference on Networking, Sensing and Control: Proceedings*, IEEE, 757–761, doi:10.1109/ICNSC.2006.1673241.

Chen, B., and Z. Liu, 2014: Voxel-optimized regional water vapor tomography and comparison with radiosonde and numerical weather model. *J. Geod.*, **88**, 691–703, doi:10.1007/s00190-014-0715-y.

Dach, R., U. Hugentobler, P. Fridez, and M. Meindl, Eds., 2007: User manual of the Bernese GPS software version 5.0. Astronomical Institute, University of Bern, 612 pp.

Dee, D. P., and Coauthors, 2011: The ERA-Interim reanalysis: Configuration and performance of the data assimilation system. *Quart. J. Roy. Meteor. Soc.*, **137**, 553–597, doi:10.1002/qj.828.

Duan, J., and Coauthors, 1996: GPS meteorology: Direct estimation of the absolute value of precipitable water. *J. Appl. Meteor.*, **35**, 830–838, doi:10.1175/1520-0450(1996)035<0830:GMDEOT>2.0.CO;2.

Elgered, G., J. M. Johansson, and B. O. Rönnäng, 1997: Measuring regional atmospheric water vapor using the Swedish permanent GPS network. *Geophys. Res. Lett.*, **24**, 2663–2666, doi:10.1029/97GL02798.

Flores, A., G. Ruffini, and A. Rius, 2000: 4D tropospheric tomography using GPS slant wet delays. *Ann. Geophys.*, **18**, 223–234, doi:10.1007/s00585-000-0223-7.

Herring, T. A., R. W. King, and S. C. McClusky, 2010: GAMIT reference manual release 10.4. Massachusetts Institute of Technology, 171 pp.

Hong Kong Observatory, 2011: Tropical cyclones in 2010. 117 pp. [Available online at http://www.weather.gov.hk/publica/tc/tc2010.pdf.]

——, 2016a: Observed climate change in Hong Kong: Extreme weather events. [Available online at http://www.weather.gov.hk/climate_change/obs_hk_extreme_weather_e.htm.]

——, 2016b: Rainstorm warning system. [Available online at http://www.hko.gov.hk/wservice/warning/rainstor.htm.]

IPCC, 2014: *Climate Change 2014: Synthesis Report*. Cambridge University Press, 151 pp.

Jessup, S. M., and A. T. DeGaetano, 2008: A statistical comparison of the properties of flash flooding and nonflooding precipitation events in portions of New York and Pennsylvania. *Wea. Forecasting*, **23**, 114–130, doi:10.1175/2007WAF2006066.1.

Jiang, P., S. R. Ye, Y. Y. Liu, J. J. Zhang, and P. F. Xia, 2014: Near real-time water vapor tomography using ground-based GPS and meteorological data: Long-term experiment in Hong Kong. *Ann. Geophys.*, **32**, 911–923, doi:10.5194/angeo-32-911-2014.

Kawano, N., O. Ito, and J.-I. Sakagami, 2008: Flash flooding resistance of rice genotypes of *Oryza sativa* L., *O. glaberrima* Steud., and Interspecific hybridization progeny. *Environ. Exp. Bot.*, **63**, 9–18, doi:10.1016/j.envexpbot.2007.12.001.

Labbouz, L., and Coauthors, 2013: Precipitation on the lee side of the Vosges Mountains: Multi-instrumental study of one case from the COPS campaign. *Meteor. Z.*, **22**, 413–432, doi:10.1127/0941-2948/2013/0413.

Lee, S.-W., J. Kouba, B. Schutz, D. H. Kim, and Y. J. Lee, 2013: Monitoring precipitable water vapor in real-time using global navigation satellite systems. *J. Geod.*, **87**, 923–934, doi:10.1007/s00190-013-0655-y.

Li, M., W. Li, C. Shi, Q. Zhao, X. Su, L. Qu, and Z. Liu, 2015: Assessment of precipitable water vapor derived from ground-based BeiDou observations with Precise Point Positioning approach. *Adv. Space Res.*, **55**, 150–162, doi:10.1016/j.asr.2014.10.010.

Li, Z., 2003: Comparison of precipitable water vapor derived from radiosonde, GPS, and Moderate-Resolution Imaging Spectroradiometer measurements. *J. Geophys. Res.*, **108**, 4651, doi:10.1029/2003JD003372.

Liu, Z., M. S. Wong, J. Nichol, and P. W. Chan, 2013: A multi-sensor study of water vapour from radiosonde, MODIS and AERONET: A case study of Hong Kong. *Int. J. Climatol.*, **33**, 109–120, doi:10.1002/joc.3412.

——, B. Chen, S. T. Chan, Y. Cao, Y. Gao, K. Zhang, and J. Nichol, 2014: Analysis and modelling of water vapour and temperature changes in Hong Kong using a 40-year radiosonde record: 1973-2012. *Int. J. Climatol.*, **35**, 462–474, doi:10.1002/joc.4001.

Lutz, S., 2009: High-resolution GPS tomography in view of hydrological hazard assessment. Astronomisch-geodätische Arbeiten in der Schweiz, Vol. 76, Swiss Geodetic Commission, 202 pp.

Manning, T., K. Zhang, W. Rohm, S. Choy, and F. Hurter, 2012: Detecting severe weather in Australia using GPS tomography. *J. Global Positioning Syst.*, **11**, 58–70, doi:10.5081/jgps.11.1.59.

Mendes, V. B., 1999: Modeling the neutral-atmosphere propagation delay in radiometric space techniques. Geodesy and Geomatics Engineering Tech. Rep. 199, University of New Brunswick, 378 pp.

Mohanakumar, K., 2008: *Stratosphere Troposphere Interactions: An introduction.* Springer, 416 pp., doi:10.1007/978-1-4020-8217-7.

Niell, A. E., 1996: Global mapping functions for the atmosphere delay at radio wavelengths. *J. Geophys. Res.*, **101**, 3227–3246, doi:10.1029/95JB03048.

——, A. J. Coster, F. S. Solheim, V. B. Mendes, P. C. Toor, R. B. Langley, and C. A. Upham, 2001: Comparison of measurements of atmospheric wet delay by radiosonde, water vapor radiometer, GPS, and VLBI. *J. Atmos. Oceanic Technol.*, **18**, 830–850, doi:10.1175/1520-0426(2001)018<0830:COMOAW>2.0.CO;2.

Ning, T., R. Haas, G. Elgered, and U. Willén, 2012: Multi-technique comparisons of 10 years of wet delay estimates on the west coast of Sweden. *J. Geod.*, **86**, 565–575, doi:10.1007/s00190-011-0527-2.

Notarpietro, R., M. Cucca, M. Gabella, G. Venuti, and G. Perona, 2011: Tomographic reconstruction of wet and total refractivity fields from GNSS receiver networks. *Adv. Space Res.*, **47**, 898–912, doi:10.1016/j.asr.2010.12.025.

Peel, M. C., B. L. Finlayson, and T. A. McMahon, 2007: Updated world map of the Köppen-Geiger climate classification. *Hydrol. Earth Syst. Sci.*, **11**, 1633–1644, doi:10.5194/hess-11-1633-2007.

Perler, D., A. Geiger, and F. Hurter, 2011: 4D GPS water vapor tomography: New parameterized approaches. *J. Geod.*, **85**, 539–550, doi:10.1007/s00190-011-0454-2.

Pilon, P. J., 2005: Guidelines for reducing flood losses. United Nations Office for Disaster Reduction, 87 pp.

Rocken, C., R. Ware, T. V. Hove, F. Solheim, C. Alber, and J. Johnson, 1993: Sensing atmospheric water vapor with the global positioning system. *Geophys. Res. Lett.*, **20**, 2631–2634, doi:10.1029/93GL02935.

Rohm, W., and J. Bosy, 2009: Local tomography troposphere model over mountains area. *Atmos. Res.*, **93**, 777–783, doi:10.1016/j.atmosres.2009.03.013.

——, K. Zhang, and J. Bosy, 2014: Limited constraint, robust Kalman filtering for GNSS troposphere tomography. *Atmos. Meas. Tech.*, **7**, 1475–1486, doi:10.5194/amt-7-1475-2014.

Ross, R. J., and W. P. Elliott, 1996: Tropospheric water vapor climatology and trends over North America: 1973–93. *J. Climate*, **9**, 3561–3574, doi:10.1175/1520-0442(1996)009<3561:TWVCAT>2.0.CO;2.

Saastamoinen, J., 1972: Atmospheric correction for the troposphere and stratosphere in radio ranging of satellites. *The Use of Artificial Satellites for Geodesy*, *Geophys. Monogr.*, Vol. 15, Amer. Geophys. Union, 247–251, doi:10.1029/GM015p0247.

Sudhir, M. S., 2003: Investigations into the estimation of tropospheric delay and wet refractivity using GPS measurements. Dept. of Geomatics Engineering, University of Calgary Rep. 20180, 142 pp.

Tregoning, P., R. Boers, D. O'Brien, and M. Hendy, 1998: Accuracy of absolute precipitable water vapor estimates from GPS observations. *J. Geophys. Res.*, **103**, 28 701–28 710, doi:10.1029/98JD02516.

Troller, M., 2004: GPS based determination of the integrated and spatially distributed water vapor in the troposphere. Astronomisch-geodätische Arbeiten in der Schweiz, Vol. 67, Swiss Geodetic Commission, 173 pp.

——, A. Geiger, E. Brockmann, J.-M. Bettems, B. Bürki, and H.-G. Kahle, 2006: Tomographic determination of the spatial distribution of water vapor using GPS observations. *Adv. Space Res.*, **37**, 2211–2217, doi:10.1016/j.asr.2005.07.002.

Van Baelen, J., and G. Penide, 2009: Study of water vapor vertical variability and possible cloud formation with a small network of GPS stations. *Geophys. Res. Lett.*, **36**, L02804, doi:10.1029/2008GL036148.

——, M. Reverdy, F. Tridon, L. Labbouz, G. Dick, M. Bender, and M. Hagen, 2011: On the relationship between water vapour field evolution and the life cycle of precipitation systems. *Quart. J. Roy. Meteor. Soc.*, **137**, 204–223, doi:10.1002/qj.785.

Webb, F. H., and J. F. Zumberge, 1997: An introduction to the GIPSY/OASIS II. JPL Publ. JPL D-11088, 15 pp.

Wong, W. K., 2010: Development of operational rapid update non-hydrostatic NWP and data assimilation systems in the Hong Kong Observatory. Hong Kong Observatory Reprint 882, 16 pp. [Available online at http://www.hko.gov.hk/publica/reprint/r882.pdf.]

Zhang, K., T. Manning, S. Wu, W. Rohm, D. Silcock, and S. Choy, 2015: Capturing the signature of severe weather events in Australia using GPS measurements. *IEEE J. Sel. Top. Appl. Earth Obs. Remote Sens.*, **8**, 1839–1847, doi:10.1109/JSTARS.2015.2406313.